Enhanced OER Performance by Cu substituted Spinel Cobalt Oxide

Leiming Tao (eimingtao@foxmail.com)
Guangdong University of Petrochemical Technology
Kui Pang
Guangdong University of Petrochemical Technology
Liming Huang
Guangdong University of Petrochemical Technology
Jiada Han
Guangdong University of Petrochemical Technology
Mengdi Zhang
Guangdong University of Petrochemical Technology
Changlin Yu
Guangdong University of Petrochemical Technology

Research Article

Keywords: Cobalt-Based Spinel, DFT, OER, Overall Water-splitting

Posted Date: July 28th, 2022

DOI: https://doi.org/10.21203/rs.3.rs-1865714/v1

Abstract

Cobaltite spinel oxides ($CuCo_2O_4$), which show electrocatalytic activity for oxygen evolution reaction (OER), are readily synthesized using a facile hydrothermal method, with a stationary ratio, uniform flower-like mesopores morphology, and high crystallinity. We have carried out first-principles calculations on the mechanism of the reaction pathway and the Gibbs free energy diagram of $CuCo_2O_4$ structures using density functional theory (DFT) and purely confirmed by experimental results. This catalyst performed an outstanding OER performance with an overpotential 230 mV at 10 mA•cm^{-2} in 1 M KOH, which was close to IrO_2 with an overpotential 190 mV at 10 mA•cm^{-2}. This work provides a facile method for electrocatalytic oxygen production with enhanced conductivity and enhanced OER by replacing cobalt with copper.

1. Introduction

With the rapid development of modern society, the demand for energy supplies becomes increasingly urgent, and the development of an efficient and clean energy supply is imperative. [1, 2] Water-splitting has been widely regarded as a promising and sustainable approach to producing clean hydrogen fuel from aqueous solutions. The gross chemical reaction is resumed as below: $H_2O \rightarrow H_2 + 1/2\ O_2$. Compared with hydrogen evolution reaction (HER), which is relatively advantageous in kinetics, oxygen evolution reaction (OER) is slower and requires higher overpotential to drive electrochemical reaction, which limits the overall water decomposition efficiency. Furthermore, O_2 production is more complex and requires more overpotential than the theoretical potential (1.23 V). [3,4,9,10] In alkaline solution, noble-metal oxides (e.g. IrO_2, RuO_2) usually serve as the OER catalysts. [5,6] However, noble metal-based electrocatalysts are difficult to commercialize on a large scale due to their high cost, poor stability, and low abundance in natural resources. [7,8,11] Therefore, many low-budget electrocatalysts based on earth-rich elements, for instance metallic oxides/hydroxides, transition metal bisuliphides, metal carbides and nitrides of transition (TMNs and MXenes), impurity atoms doped carbon, layered double hydroxides (LDHs), Metallic organic framework (MOFs), single element catalysts, have been exploited to substitute for precious metal electrocatalysts for water decomposition. [18–35]

In the past decades, Ternary transition metal oxides such as spinel containing different metal cations promise electrochemical active materials, which might be employed in lithium-ion batteries, supercapacitors and electrocatalysts. [12] Due to its richer redox reaction and lower electron transfer activation energy than single metal oxides, spinel demonstrates greater electrochemical performance. $CuCo_2O_4$ has attracted wide attention among different spinels as a promising electrochemical electrode material. This is due to the low price, non-toxicity and the synergistic effect of cobalt and copper species as high conductivity species. Up to now, various shapes of $CuCo_2O_4$ materials such as nanowires, nanometer grass, nanometer flakes, nanometer cubes, hollow spheres, double-shell hollow spheres and nanotubes have been used to prepare electrodes. [36–42]

As one of the well-known $CuCo_2O_4$ has been investigated extensively as a corrosion-stable and highly efficient catalyst for OER in alkaline media. For other spinel materials, $MxCo_{3-x}O_4$ materials (M = Mn, Ni, Fe, Zn). After Cu replaces cobalt, the conductivity and charge transfer ability are significantly improved, thereby promoting OER performance under alkaline conditions. [3–5]

The combination of the theoretical and experimental approaches towards the different active of $CuCo_2O_4$ was conducted. In the experiment, the ratio, morphology and crystal structure of elements Cu and Co will all affect the oxygen production performance of $CuCo_2O_4$ electrolytic water. Although DFT has succeeded in some simulation materials, it is not precise enough to calculate the electronic structure of the transition metal.[6–8] It is challenging for the experiment and theoretical calculations.

In the present work, we report that cobaltite spinel oxides $CuCo_2O_4$ was readily synthesized using a facile hydrothermal method, with a stationary ratio (Cu/Co = 1/2), uniform flower-like mesopores morphology, and high crystallinity. Under theoretical prediction and experimental results, we found that $CuCo_2O_4$ shows the best electrocatalytic activity. The catalyst exhibits excellent OER performance in 1 M KOH with an overpotential of 230 mV at 10 $mA•cm^{-2}$, which is close to IrO_2 with an overpotential of 190 mV at 10 $mA•cm^{-2}$.

2. Experimental Section

Synthesis of MCo_2–PTCDA MMOFs is based on the method in ref. with some modification. The detailed procedure is as follows.

2.1 Preparation of the $CuCo_2$-PTCDA.

$Cu(OAc)_2·2H_2O$ (0.133 mmol) and $Co(OAc)_2·4H_2O$ (0.267 mmol) were dissolved in 22.5 mL deionized water, and PTCDA (0.2 mmol) was dissolved in 12.5 mL NaOH solution (0.8 mmol NaOH). The PTCDA solution was added dropwise to the mixture solution of metal acetates with stirring. The immediate formation of a precipitate was observed. The reaction mixture was stirred at room temperature for 30 min, and then transferred to a Teflon-lined stainless steel vessel (45 mL) and heated at 100°C for 8 h. After cooling down to room temperature, the precipitate was collected by centrifugation, washed with water and dried.

2.2 Preparation of the $CuCo_2$-PTCDA

For other $CuCo_2$–PTCDA MMOFs, the synthesis process was similar to that described for $CuCo_2$–PTCDA except using M(II) acetate instead of cobalt(III) acetate.

2.3 Preparation of the $CuCo_2O_4$

Formation of $CuCo_2O_4$ nanomaterials $CuCo_2$–PTCDA MMOFs were thermally treated in air at 550°C for 1 h with a ramp of 1°C •min^{-1}.

2.4 Characterization

The morphology, chemical composition, and structure of samples were characterized by high resolution field emission scanning electron microscopy (FESEM, Nova NanoSEM 450), transmission electron microscopy (TEM, 300 kV Titan Probe corrected TEM, Titan G2 60–300), and XPS (Thermo fisher-ESCALab 250). The Brunauer-Emmett-Teller (BET) surface area (SBET) and pore size distribution were determined using a Micromeritics ASAP 2000 nitrogen adsorption apparatus. All the samples were degassed at 180°C prior to BET measurements.

2.5 Electrode fabrication and performance measurements

For the electrode preparation, 2 mg of $CuCo_2O_4$ powder was dispersed into a 1 mL mixture of water, ethanol and Nafion (5 wt. % solution in a mixture of lower aliphatic alcohols and water, Aldrich) with the volume ratio of 1:3.85:0.15 by ultrasonication for 30 min. This afforded a catalyst ink of concentration 2.0 mg•mL^{-1}. Afterwards, 7 µL (19.8 µL) of the suspension was transferred onto the polished 3 mm (5 mm) in diameter glassy-carbon electrode, giving a mass loading of 0.2 mg•cm^{-2}.

The cyclic voltammetry (CV) and linear sweep voltammetry (LSV) measurements were conducted with an electrochemical station (CHI 750D), in which the GC electrode (3 mm in diameter, Chenhua Co. Shanghai) was used as the working electrode, a carbon electrode as the auxiliary electrode, and a Hg/HgO as the reference electrode. An Autolab PGSTAT302N measured the electrochemical impedance spectroscopy at a frequency ranging from 1 mHz to 1 MHz with a potential amplitude of 10 mV.

Electrochemical measurements were conducted in 1 M KOH electrolyte at room temperature using a three-electrode system (Pine Instruments and WaveDriver Workstation). All potentials were measured versus a Hg/HgO, and a carbon electrode was used as the counter electrode. Several cyclic voltammetry cycles were taken from 0 to 0.8 V (vs Hg/HgO) to stabilize the HER and OER performance of the catalyst before polarization curves were recorded. Recently, it has been reported that the amount of Pt deposited on catalyst surface after multiple circular scanning improves the catalytic performance. Therefore, a carbon electrode was used as the counter electrode in this study. Then, the polarization curves and Tafel plots were recorded at scan rates of 5 mV• s^{-1} and 0.1 mV• s^{-1}, respectively. The solution impedance (R) of 1M KOH measured was 6.9 Ω at room temperature. Accurate Tafel plots of samples were obtained according to a previous method. This was conducted seven times with altering rotation speeds (400 r.p.m., 620 r.p.m., 900 r.p.m., 1225 r.p.m., 1600 r.p.m., 2025 r.p.m., 2500 r.p.m., respectively).

The turnover frequency (TOF) was evaluated by the following standard equation:

$$\mathrm{TOF} = \frac{J \times A}{4 \times F \times \mathrm{m}}$$

Here, J is the current density ($A \cdot cm^{-2}$) at an overpotential of 0.3V. A and m are the area of the electrode and the number of moles of the active materials that were deposited onto the electrode, respectively. F is the Faraday constant (96,485 $C \cdot mol^{-1}$).

The Faradaic efficiency (FE) was obtained according to the previous literature:

$$FE = \frac{Iring}{Ce \times Idisk}$$

Here, I_{disk} is the given current on the disk electrode. I_{ring} is the collection current on the Pt ring electrode at a constant potential of 0.4 V versus RHE. C_e is the oxygen collection coefficient (~ 0.2) for this type of electrode configuration.

2.6 Gas chromatography measurement.

The working electrode with the catalyst was prepared by drop-drying 0.2 mg catalyst onto a freshly polished glassy-carbon electrode (diameter = 0.5 cm).

Chronopotentiometry was applied with a given potential (1.53V and − 0.3V) to maintain constant O_2 and H_2 generation. N_2 was constantly purged into the cathodic compartment at a flow rate of $5cm^3 \cdot min^{-1}$, and the compartment was connected to the gas-sampling loop of a gas chromatograph (GC2020, Hubei Hengxinshiji Scientific Instrument Co.). A thermal conductivity detector (TCD) was used to detect and quantify the generated O_2 and H_2.

2.7 Density Functional Theory (DFT) Calculation

The optimal cell structure of Co_2CuO_4 was derived by MedeA software. The (100) surface of Co_2CuO_4 was established by using the software ' Build Surface ' function and calculated by Vienna ab initio simulation package (VASP) based on density functional theory and GGA-PBE exchange correlation functional. Because there is no magnetic moment in the model, it is a nonmagnetic calculation with ' normal ' accuracy. Conjugate Gradient algorithm is used and the convergence criterion is 0.02 eV per e. The default plane wave cut-off energy is 400.000 eV. The K-point spacing is set to 0.5 per Å (0.51 / Ang) and the k-grid is forced to be gamma-point center. At the same time, the Guass method with a width of 0.05 eV is used for integration, and the final electron self-consistent field method, standard is set to 10^{-5} eV.

After calculating the energy of the substrate, adsorbed molecule, and surface adsorbed state, the adsorption energy is calculated by the following formula:

$$\mathrm{E}= E_{ads} - E_{surface} - E_{molecular}$$

If the positive value indicates that it is difficult to adsorb, the energy obtained after adsorption is higher than the individual energy. Negative value means exothermic, adsorption system is more stable, lower

energy.

3. Results And Discussion

Diffraction peaks at 2θ values of 31.3°, 36.9°, 44.9°, 59.5°, and 65.4° are observed in Fig. 1a for $CuCo_2O_4$, which correspond to the lattice planes of (2 2 0), (3 1 1), (4 0 0), (5 1 1), and (4 4 0) of the $CuCo_2O_4$ phase, indicating the formation of $CuCo_2O_4$ crystallites (ICSD: 01-1155).

The FE-SEM image reveals that the resulting $CuCo_2O_4$ material is composed of nanoplate assemblies inherited from the $CuCo_2$–PTCDA precursor with flower-like morphology (Fig. 1b). The nanoplates, which assemble to form the flower-like morphology, are porous under the observation of the TEM image (Fig. 1c). The transmission electron microscopy (TEM) and selected area electron diffraction (SAED) analysis of an isolated nanoplate display polycrystal properties with periodic diffraction spots (Fig. 1e). The particle size of the nanoplate is about 1.6 μm. The six marked diffraction rings correspond to the (1 1 1), (2 2 0), (3 1 1), (2 2 2), (5 1 1), and (4 4 0) planes. Furthermore, Fig. 1d displays a representative HR-TEM image of the $CuCo_2O_4$ nanoparticles. The nanoplates are composed of nanoparticles with a particle size of about 12 nm. They are well-crystallized in the cubic phase, with the (3 1 1) crystal lattice having interplane spacings of 0.24 nm, which is consistent with the (3 1 1) highest diffraction peak of XRD patterns of $CuCo_2O_4$.

The SEM image along with the EDX pattern of a representative composition $CuCo_2O_4$, shown in Fig. 2, shows the presence of C, O, Cu and Co. The EDX mappings reveal that copper and cobalt elements are homogeneously distributed in the whole $CuCo_2O_4$ sample. Quantitative elemental composition analysis of the CuCoO electro-catalysts of different compositions obtained by EDX composition showed that the measured elemental compositions of Cu and Co are in close agreement with the nominal composition.

The thermal transformation process from MMOFs to spinel structured mixed-metal oxide was investigated by thermogravimetric (TG) analysis using $CuCo_2$–PTCDA as a model (Fig. 3a). The sample has two consecutive weight loss steps. The preliminary weight loss at 350℃ corresponds to the escape of perylene by decarboxylation. There is a well-defined weight loss due to the oxygen release of $CuCo_2O_4$ thermal decomposition above 650℃. The spinel structure could not be formed at treatment temperatures below 450℃.

Figure 3b is the FTIR spectra of the PTCDA, $CuCo_2$-PTCDA and $CuCo_2O_4$ electrode materials in the range of 1000–2000 cm^{-1}. The peaks at 1296, 1770 and 1400 ~ 1600 cm^{-1} are attributed to the cyclic anhydride C-O deformation of PTCDA, cyclic anhydride C = O stretching vibration and phenyl C = C vibration. The FTIR peaks of cyclic anhydride C = O stretching vibration (1776 cm^{-1}) and C-O stretching vibration (1296 cm^{-1}) disappeared after $CuCo_2O_4$ was recombined on PTCDA by cyclic anhydride. [43]

These oxides showed considerably improved specific surface area and apparent electrocatalytic activity. The surface area of porous structured $CuCo_2O_4$ was characterized N_2 sorption measurements as shown in Fig. 3c. The samples for $CuCo_2O_4$ had the specific Brunauer-Emmett-Teller (BET) surface area of 49.44 $m^2 \cdot g^{-1}$ and uniform distribution of the mesopores with pore diameter of 14.8 nm, respectively. The result of BET corresponded with the previous report. [44–45]

Using cyclic voltammetry,C_{dl} values were more straightforwardly estimated from the slope of the linear charging current i_{cp} vs scan rate v plots obtained by recording cyclic voltammograms in a narrow potential region of 50 mV, i.e. of ± 25 mV around the same potentials as above. CV curves were performed without a redox process from 0 to 0.05 V (ranging from 10 to 120 $mV \bullet s^{-1}$(Fig. 3d)). According to the CV curves and the plots of the resultant current densities versus scan rates, the C_{dl} of $CuCo_2O_4$ is determined to be 1.0 $mF \bullet cm^{-2}$. C_{dl} is related to the surface area. Large ECSA is conducive to the adsorption of water molecules and the rich active sites in the electrochemical reaction process.

Surface chemical composition and element oxidation states of the $CuCo_2O_4$ MMOFs were analyzed using XPS. Figure 4a displays the C 1s spectrum of $CuCo_2O_4$ MMOFs. The peaks at 288.4 and 286 eV are assigned to the O–C = O and C–O–C from the pure PTCDA cyclic anhydride, whereas the peak at 284.4 eV is assigned to the C–C. Figure 4b shows the O 1s spectrum of $CuCo_2O_4$ MMOFs. The peaks at 533.6, 532, and 530.5 eV are assigned to the O–C = O, C = O, and C–O from the PTCDA cyclic anhydride, whereas the peak at 529.1 eV is assigned to the M–O (where M represents the metal). In the Cu 2p spectra (Fig. 4(c)), three types of Cu species are detected. The peaks at 932 and 952 eV are ascribed to Cu^{2+}. In the Co 2p spectra (Fig. 4d), two types of Co species (Co^{2+} and Co^{3+}) are obtained. The binding energies at 782.1 and 797.5 eV are ascribed to Co^{2+}. Another two fitting peaks at 780.1 and 795.4 eV are ascribed to Co^{3+}. These results indicate the co-existence of the Co(II) and Co(III) in $CuCo_2O_4$ (e.g., Co^{3+}/Co^{2+} ratio = 2.0, estimated from the ratio between the corresponding peak areas).

To verify the theory prediction, we tested electrochemical activity. The electrocatalytic activities of $CuCo_2O_4$ for the OER were tested by loading the samples onto a glassy carbon electrode that served as the working electrode. The linear sweep voltammetry (LSV) was evaluated using a three-electrode electrochemical cell in a 1.0 M KOH solution. Under similar alkaline conditions, Fig. 5 shows the OER and Tafel slope. IrO_2 and $CuCo_2O_4$ are for the OER with overpotentials at 190 mV and 230 mV, and with the Tafel slope of 79.7 and 80.7 $mV \bullet dec^{-1}$, respectively. It is consistent with the theory prediction.

The above potentials were chosen to belong to the ideally polarized (i.e. flat) region (0–0.05 V) of the CV curves, wherein faradaic processes and surface redox pseudo-capacitances can be assumed to be negligible. A typical Bode plot for $CuCo_2O_4$ recorded at E = 50 mV vs. Hg/HgO is shown in Fig. 5c as an example. The impedance further proved the charge transfer ability, and then the catalytic activity was evaluated (Fig. 5d). It can be seen that there are differences among different metal oxide electrodes, from Pt20%C (6.67 olm), $CuCo_2O_4$ (16.67 olm) to the highest $ZnCo_2O_4$ (133.33 olm), so $CuCo_2O_4$ has good

conductivity and charge transfer ability. This has been reported in previous articles and can be well confirmed. [46,47]

The three $CuCo_2O_4$ materials with different electronic structures, similar morphology and geometrical surface area provided the opportunity to study the relationship between crystal structure and electrocatalytic activity. [48–50]

Figure 6a shows the $CuCo_2O_4$ model diagram. The electrons can pass through the Fermi level and can move freely to enhance the conductivity (Fig. 6b). However, the electrons fail to pass through the Fermi level, and the electron movement is hindered, resulting in poor conductivity (Fig. 6d). We begin with calculations to understand and identify active sites that favor high activity for hydrogen and oxygen evolution. In order to reveal the structural advantages of hydrogen and oxygen evolution of $CuCo_2O_4$, density functional theory (DFT) was used to analyze the mechanism of the reaction pathway and the Gibbs free energy diagram (see method for details) was obtained. Based on the experimental results and in order to provide supporting information on the reaction pathway, different adsorption orientations of the intermediates at all possible active sites were determined. The first step in electrochemical reduction of H_2O is adsorption of the target molecule. The likelihood estimation is performed for each reaction according to the energy difference of ΔG_H values before and after each reaction. As shown in the Fig. 6c, in the alternating mechanism, the adsorption energy of the *OOH intermediate of Cu on the surface of $CuCo_2O_4$ is 2.39 eV, which is the energy required for the rate-decision step.

4. Conclusion

In short, this work introduces copper cobaltate nanoflowers for high-performance oxygen production. The newly designed $CuCo_2O_4$ catalyst puts up an overpotential of 230 mV at 10 $mA{\cdot}m^{-2}$ for OER electrocatalytic activity in 1M KOH solution. Tafel slope 79.7 $mV{\bullet}dec^{-1}$ lower than IrO_2 80.7 $mV{\bullet}dec^{-1}$. DFT calculation shows that the decisive step of electrocatalytic oxygen production is *O→*OOH. The required energy is 2.39 eV, which is consistent with experimental results. This is superior to the reported electrochemical activity. This research enhances its OER performance by replacing cobalt with copper to increase conductivity, which provides a direction for non-noble metal oxygen-producing catalysts.

Declarations

Funding

The authors gratefully acknowledge financial support from the National Basic Research Program of China (22078072), the Featured Innovation Project of Guangdong Education Department (2021ZDZX4060), Scientific Research Fund of Natural Science Foundation of Guangdong University of Petrochemical Technology (2019rc019, 2019rc011), Science and technology project of Maoming City (2020578, 2020526 and 2021018).

Authors' Information

Authors and Affiliations

Authors: Leiming Tao [a], Kui Pang[a,b], Liming Huang[a,c], Jiada Han[a], Mengdi Zhang[a], Changlin Yu[a]

Affiliations:

[a] Guangdong Provincial Key Laboratory of Petrochemical Equipment Fault Diagnosis, School of Science, Guangdong University of Petrochemical Technology, Maoming, Guangdong, 525000, China.

[b] Engineering Research Center for Nanomaterials, Henan University, Henan 475001, China

[c] School of Chemistry and Chemical Engineering, Guangxi University, Nanning 530000, China

Correspondence to Leiming Tao (Email: leimingtao@foxmail.com).

Consent to participate

All authors approved the version to be published.

Author Contributions

L. T. designed the experiments. K.P and L.H. helped to perform characterization and electrochemical measurements. H.J helped with the calculations by VASP. L.T., M.Z. and C. Y. analyzed the data and modified the manuscript. L.T. supervised the experiment.

Ethics Declarations

We declare that we have no financial and personal relationships with other people or organizations that can inappropriately influence our work, there is no professional or other personal interest of any nature or kind in any product, service and/or company that could be construed as influencing the position presented in, or the review of, the manuscript entitled.

Conflict of Interest

The authors declare no competing interests.

Consent for publication

I have read the Springer journal policies on author responsibilities and submit this manuscript in accordance with those policies. I declare that the authors have no competing interests as defined by Springer, or other interests that might be perceived to influence the results and/or discussion reported in this paper.

Availability of data and material

The results/data/figures in this manuscript have not been published elsewhere, nor are they under consideration by another publisher.

Additional information

Publisher's Note

Springer Nature remains neutral with regard to jurisdictional claims in published maps and institutional affiliations.

Rights and permissions

All of the material is owned by the authors and/or no permissions are required.

References

1. T. Wu, S. Sun, J. Song, S. Xi, Y. Du, B. Chen, W.A. Sasangka, H. Liao, C.L. Gan, G.G. Scherer, L. Zeng, H. Wang, H. Li, A. Grimaud, Z.J. Xu, Iron-facilitated dynamic active-site generation on spinel $CoAl_2O_4$ with self-termination of surface reconstruction for water oxidation, Nature Catalysis, 2 (2019) 763–772.
2. D. Zhao, M. Dai, Y. Zhao, H. Liu, Y. Liu, X. Wu, Improving electrocatalytic activities of $FeCo_2O_4$@$FeCo_2S_4$@PPy electrodes by surface/interface regulation, Nano Energy, 72 (2020).
3. J. Li, G. Zheng, One-Dimensional Earth-Abundant Nanomaterials for Water-Splitting Electrocatalysts, Adv Sci (Weinh), 4 (2017) 1600380.
4. Y. Jiao, Y. Zheng, M. Jaroniec, S.Z. Qiao, Design of electrocatalysts for oxygen- and hydrogen-involving energy conversion reactions, Chem Soc Rev, 44 (2015) 2060–2086.
5. Y. Li, Y. Wang, J. Lu, B. Yang, X. San, Z.-S. Wu, 2D intrinsically defective RuO_2/Graphene heterostructures as All-pH efficient oxygen evolving electrocatalysts with unprecedented activity, Nano Energy, 78 (2020).
6. J. Chen, P. Cui, G. Zhao, K. Rui, M. Lao, Y. Chen, X. Zheng, Y. Jiang, H. Pan, S.X. Dou, W. Sun, Low-Coordinate Iridium Oxide Confined on Graphitic Carbon Nitride for Highly Efficient Oxygen Evolution, Angew Chem Int Ed Engl, 58 (2019) 12540–12544.
7. X. Zou, Y. Zhang, Noble metal-free hydrogen evolution catalysts for water splitting, Chem Soc Rev, 44 (2015) 5148–5180.
8. C. Zhu, A.L. Wang, W. Xiao, D. Chao, X. Zhang, N.H. Tiep, S. Chen, J. Kang, X. Wang, J. Ding, J. Wang, H. Zhang, H.J. Fan, In Situ Grown Epitaxial Heterojunction Exhibits High-Performance Electrocatalytic Water Splitting, Adv Mater, 30 (2018) e1705516.
9. A.T. Aqueel Ahmed, B. Hou, H.S. Chavan, Y. Jo, S. Cho, J. Kim, S.M. Pawar, S. Cha, A.I. Inamdar, H. Kim, H. Im, Self-Assembled Nanostructured CuCo2 O4 for Electrochemical Energy Storage and the Oxygen Evolution Reaction via Morphology Engineering, Small, 14 (2018) e1800742.

10. Principles of Water Electrolysis and Recent Progress in Cobalt-, Nickel-, and Iron-Based Oxides for the Oxygen Evolution Reaction, Angew Chem Int Ed Engl, 61 (2022) e202103824.
11. Z. Kou, K. Wang, Z. Liu, L. Zeng, Z. Li, B. Yang, L. Lei, C. Yuan, Y. Hou, Recent Advances in Manifold Exfoliated Synthesis of Two-Dimensional Non-precious Metal-Based Nanosheet Electrocatalysts for Water Splitting, Small Structures, 3 (2021).
12. Engineering onion-like nanoporous $CuCo_2O_4$ hollow spheres derived from bimetal–organic frameworks for high-performance asymmetric supercapacitors, Journal of Materials Chemistry A, 6 (2018) 10497–10506.
13. G. Wei, J. He, W. Zhang, X. Zhao, S. Qiu, C. An, Rational Design of Co(II) Dominant and Oxygen Vacancy Defective $CuCo_2O_4$@CQDs Hollow Spheres for Enhanced Overall Water Splitting and Supercapacitor Performance, Inorg Chem, 57 (2018) 7380–7389.
14. K. Song, W. Ai, Y. Zhang, Y. Zeng, Y. Yu, H. Qiao, Z. Liu, X. Shen, X. Hu, X. Hu, Three-dimensional self-supported $CuCo_2O_4$ nanowires@NiO nanosheets core/shell arrays as an oxygen electrode catalyst for Li–O_2 batteries, Journal of Materials Chemistry A, 9 (2021) 3007–3017.
15. P. Zhang, H. He, Rational rope-like $CuCo_2O_4$ nanosheets directly on Ni foam as multifunctional electrodes for supercapacitor and oxygen evolution reaction, Journal of Alloys and Compounds, 826 (2020).
16. A. Serov, N.I. Andersen, A.J. Roy, I. Matanovic, K. Artyushkova, P. Atanassov, $CuCo_2O_4$ ORR/OER Bi-Functional Catalyst: Influence of Synthetic Approach on Performance, Journal of The Electrochemical Society, 162 (2015) F449-F454.
17. A.T. Aqueel Ahmed, B. Hou, H.S. Chavan, Y. Jo, S. Cho, J. Kim, S.M. Pawar, S. Cha, A.I. Inamdar, H. Kim, H. Im, Self-Assembled Nanostructured $CuCo_2$ O_4 for Electrochemical Energy Storage and the Oxygen Evolution Reaction via Morphology Engineering, Small, 14 (2018) e1800742.
18. X. Zheng, Y. Chen, X. Zheng, G. Zhao, K. Rui, P. Li, X. Xu, Z. Cheng, S.X. Dou, W. Sun, Electronic Structure Engineering of $LiCoO_2$ toward Enhanced Oxygen Electrocatalysis, Advanced Energy Materials, 9 (2019).
19. K. Huang, Z. Zhao, H. Du, P. Du, H. Wang, R. Wang, S. Lin, H. Wei, Y. Long, M. Lei, W. Guo, H. Wu, Rapid Thermal Annealing toward High-Quality 2D Cobalt Fluoride Oxide as an Advanced Oxygen Evolution Electrocatalyst, ACS Sustainable Chemistry & Engineering, 8 (2020) 6905–6913.
20. M. Huynh, D.K. Bediako, D.G. Nocera, A functionally stable manganese oxide oxygen evolution catalyst in acid, J Am Chem Soc, 136 (2014) 6002–6010.
21. X. Hou, H. Zhou, M. Zhao, Y. Cai, Q. Wei, MoS_2 Nanoplates Embedded in Co–N-Doped Carbon Nanocages as Efficient Catalyst for HER and OER, ACS Sustainable Chemistry & Engineering, 8 (2020) 5724–5733.
22. H. Xue, H. Zhang, S. Fricke, M. Lüther, Z. Yang, A. Meng, W. Bremser, Z. Li, Scalable and energy-efficient synthesis of Co_xP for overall water splitting in alkaline media by high energy ball milling, Sustainable Energy & Fuels, 4 (2020) 1723–1729.

23. Z. Chen, X. Duan, W. Wei, S. Wang, B.-J. Ni, Recent advances in transition metal-based electrocatalysts for alkaline hydrogen evolution, Journal of Materials Chemistry A, 7 (2019) 14971–15005.
24. J. Luxa, Š. Cintl, L. Spejchalová, J.-Y. Lin, Z. Sofer, Potential Dependent Electrochemical Exfoliation of $NiPS_3$ and Implications for Hydrogen Evolution Reaction, ACS Applied Energy Materials, 3 (2020) 11992–11999.
25. H. Jin, Q. Gu, B. Chen, C. Tang, Y. Zheng, H. Zhang, M. Jaroniec, S.Z. Qiao, Molten Salt-Directed Catalytic Synthesis of 2D Layered Transition-Metal Nitrides for Efficient Hydrogen Evolution, Chem, 6 (2020) 2382–2394.
26. P. Urbankowski, B. Anasori, T. Makaryan, D. Er, S. Kota, P.L. Walsh, M. Zhao, V.B. Shenoy, M.W. Barsoum, Y. Gogotsi, Synthesis of two-dimensional titanium nitride Ti_4N_3 (MXene), Nanoscale, 8 (2016) 11385–11391.
27. J. Lee, S. Noh, N.D. Pham, J.H. Shim, Top-down synthesis of S-doped graphene nanosheets by electrochemical exfoliation of graphite: Metal-free bifunctional catalysts for oxygen reduction and evolution reactions, Electrochimica Acta, 313 (2019) 1–9.
28. J. Duan, S. Chen, M. Jaroniec, S.Z. Qiao, Heteroatom-Doped Graphene-Based Materials for Energy-Relevant Electrocatalytic Processes, ACS Catalysis, 5 (2015) 5207–5234.
29. Z. Yuan, J. Li, M. Yang, Z. Fang, J. Jian, D. Yu, X. Chen, L. Dai, Ultrathin Black Phosphorus-on-Nitrogen Doped Graphene for Efficient Overall Water Splitting: Dual Modulation Roles of Directional Interfacial Charge Transfer, J Am Chem Soc, 141 (2019) 4972–4979.
30. M.S. Islam, M. Kim, X. Jin, S.M. Oh, N.-S. Lee, H. Kim, S.-J. Hwang, Bifunctional 2D Superlattice Electrocatalysts of Layered Double Hydroxide–Transition Metal Dichalcogenide Active for Overall Water Splitting, ACS Energy Letters, 3 (2018) 952–960.
31. R. Liu, Y. Wang, D. Liu, Y. Zou, S. Wang, Water-Plasma-Enabled Exfoliation of Ultrathin Layered Double Hydroxide Nanosheets with Multivacancies for Water Oxidation, Adv Mater, 29 (2017).
32. F. Li, J. Li, L. Zhou, S. Dai, Enhanced OER performance of composite Co–Fe-based MOF catalysts via a one-pot ultrasonic-assisted synthetic approach, Sustainable Energy & Fuels, 5 (2021) 1095–1102.
33. K. Jayaramulu, J. Masa, D.M. Morales, O. Tomanec, V. Ranc, M. Petr, P. Wilde, Y.T. Chen, R. Zboril, W. Schuhmann, R.A. Fischer, Ultrathin 2D Cobalt Zeolite-Imidazole Framework Nanosheets for Electrocatalytic Oxygen Evolution, Adv Sci (Weinh), 5 (2018) 1801029.
34. K. Bai, J.-C. Fan, P.-H. Shi, Y.-L. Min, Q.-J. Xu, Directly ball milling red phosphorus and expended graphite for oxygen evolution reaction, Journal of Power Sources, 456 (2020).
35. R. Gusmao, Z. Sofer, D. Bousa, M. Pumera, Pnictogen (As, Sb, Bi) Nanosheets for Electrochemical Applications Are Produced by Shear Exfoliation Using Kitchen Blenders, Angew Chem Int Ed Engl, 56 (2017) 14417–14422.
36. A. Pendashteh, S.E. Moosavifard, M.S. Rahmanifar, Y. Wang, M.F. El-Kady, R.B. Kaner, M.F. Mousavi, Highly Ordered Mesoporous $CuCo_2O_4$ Nanowires, a Promising Solution for High-Performance

Supercapacitors, Chemistry of Materials, 27 (2015) 3919–3926.
37. J. Cheng, H. Yan, Y. Lu, K. Qiu, X. Hou, J. Xu, L. Han, X. Liu, J.-K. Kim, Y. Luo, Mesoporous $CuCo_2O_4$ nanograsses as multi-functional electrodes for supercapacitors and electro-catalysts, Journal of Materials Chemistry A, 3 (2015) 9769–9776.
38. S. Liu, K.S. Hui, K.N. Hui, Flower-like Copper Cobaltite Nanosheets on Graphite Paper as High-Performance Supercapacitor Electrodes and Enzymeless Glucose Sensors, ACS Appl Mater Interfaces, 8 (2016) 3258–3267.
39. W. Kang, Y. Tang, W. Li, Z. Li, X. Yang, J. Xu, C.S. Lee, Porous $CuCo_2O_4$ nanocubes wrapped by reduced graphene oxide as high-performance lithium-ion battery anodes, Nanoscale, 6 (2014) 6551–6556.
40. S.K. Kaverlavani, S.E. Moosavifard, A. Bakouei, Designing graphene-wrapped nanoporous $CuCo_2O_4$ hollow spheres electrodes for high-performance asymmetric supercapacitors, Journal of Materials Chemistry A, 5 (2017) 14301–14309.
41. S. Kamari Kaverlavani, S.E. Moosavifard, A. Bakouei, Self-templated synthesis of uniform nanoporous $CuCo_2O_4$ double-shelled hollow microspheres for high-performance asymmetric supercapacitors, Chem Commun (Camb), 53 (2017) 1052–1055.
42. J. Zhao, M. Li, J. Sun, L. Liu, P. Su, Q. Yang, C. Li, Metal-oxide nanoparticles with desired morphology inherited from coordination-polymer precursors, Chemistry, 18 (2012) 3163–3168.
43. L. Tao, M. Huang, S. Guo, Q. Wang, M. Li, X. Xiao, G. Cao, Y. Shao, Y. Shen, Y. Fu, M. Wang, Surface modification of $NiCo_2Te_4$ nanoclusters: a highly efficient electrocatalyst for overall water-splitting in neutral solution, Applied Catalysis B: Environmental, 254 (2019) 424–431.
44. J. Zhao, M. Li, J. Sun, L. Liu, P. Su, Q. Yang, C. Li, Metal-oxide nanoparticles with desired morphology inherited from coordination-polymer precursors, Chemistry, 18 (2012) 3163–3168.
45. S. Liu, L. Hu, X. Xu, A.A. Al-Ghamdi, X. Fang, Nickel Cobaltite Nanostructures for Photoelectric and Catalytic Applications, Small, 11 (2015) 4267–4283.
46. L. Tao, P. Guo, W. Zhu, T. Li, X. Zhou, Y. Fu, C. Yu, H. Ji, Highly efficient mixed-metal spinel cobaltite electrocatalysts for the oxygen evolution reaction, Chinese Journal of Catalysis, 41 (2020) 1855–1863.
47. X. Han, H. Sheng, C. Yu, T.W. Walker, G.W. Huber, J. Qiu, S. Jin, Electrocatalytic Oxidation of Glycerol to Formic Acid by $CuCo_2O_4$ Spinel Oxide Nanostructure Catalysts, ACS Catalysis, 10 (2020) 6741–6752.
48. S. Lee, J.-H. Jang, I. Jang, D. Choi, K.-S. Lee, D. Ahn, Y.S. Kang, H.-Y. Park, S.J. Yoo, Development of robust Pt shell through organic hydride donor in PtCo@Pt core-shell electrocatalysts for highly stable proton exchange membrane fuel cells, Journal of Catalysis, 379 (2019) 112–120.
49. L. Fang, Z. Jiang, H. Xu, L. Liu, Y. guan, X. Gu, Y. Wang, Crystal-plane engineering of $NiCo_2O_4$ electrocatalysts towards efficient overall water splitting, Journal of Catalysis, 357 (2018) 238–246.

50. X. Peng, X. Jin, B. Gao, Z. Liu, P.K. Chu, Strategies to improve cobalt-based electrocatalysts for electrochemical water splitting, Journal of Catalysis, 398 (2021) 54–66.

Figures

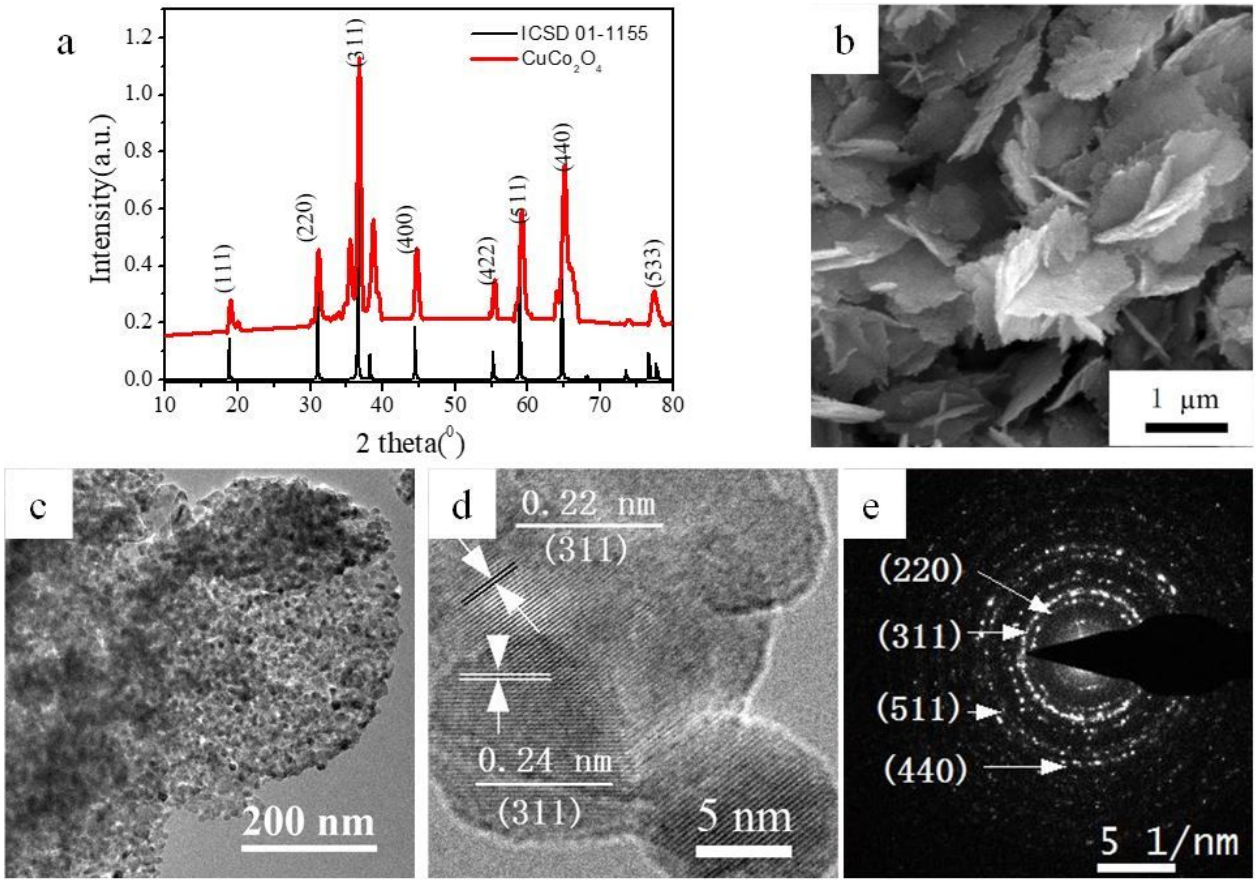

Figure 1

a) Typical XRD of spinel a $CuCo_2O_4$, b) FE-SEM images, c) Low TEM and d) HRTEM images of $CuCo_2O_4$ nanoparticles, respectively, e) with corresponding SAED

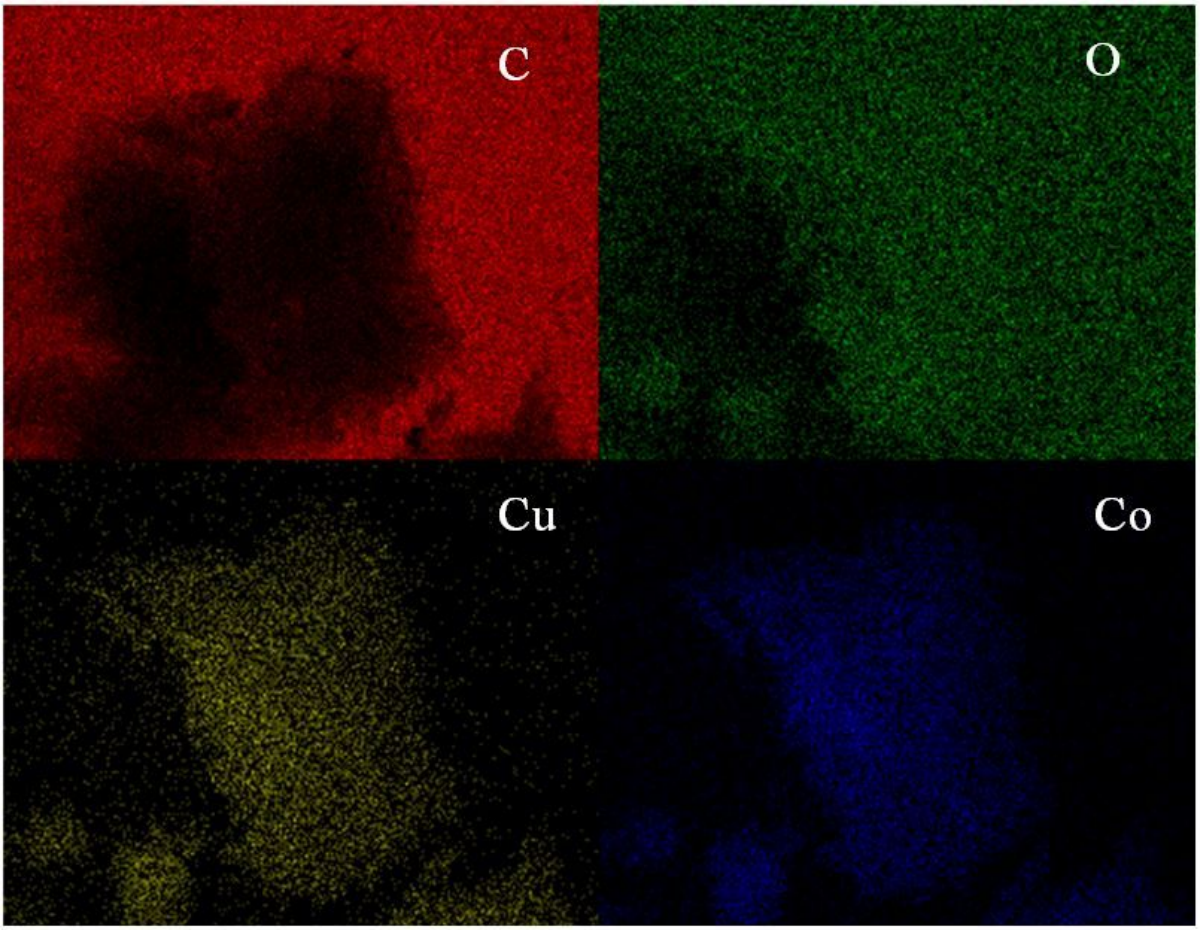

Figure 2

SEM micrograph with elemental X-ray mapping and the EDX spectrum of $CuCo_2O_4$

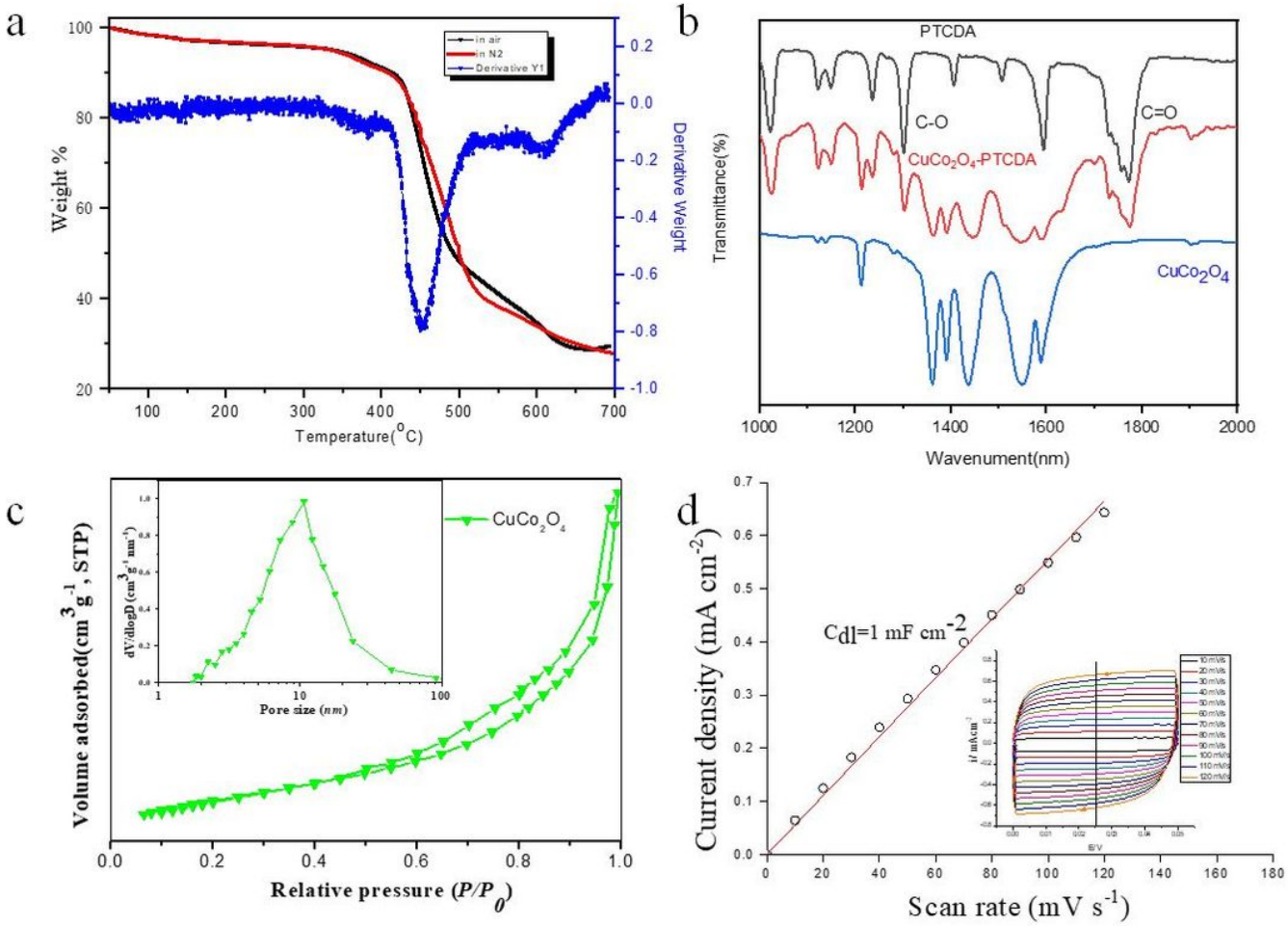

Figure 3

3a) TG curve of $CuCo_2$-ptcda in air and in N_2 and air; 3b) FT-IR Spectrum of PTCDA, $CuCo_2$-PTCDA and $CuCo_2O_4$; 3c) N_2 absorption-desorption isotherm of $CuCo_2O_4$ and inset shows the corresponding pore size distribution; 3d) Typical cyclic voltammograms and linear icap vs. scan rate, v, plots in the potential region 0-0.05 V vs. HgO/Hg, in 1M KOH at 25 °C: $CuCo_2O_4$ electrode (geometrical area: 0.07065 cm^2)

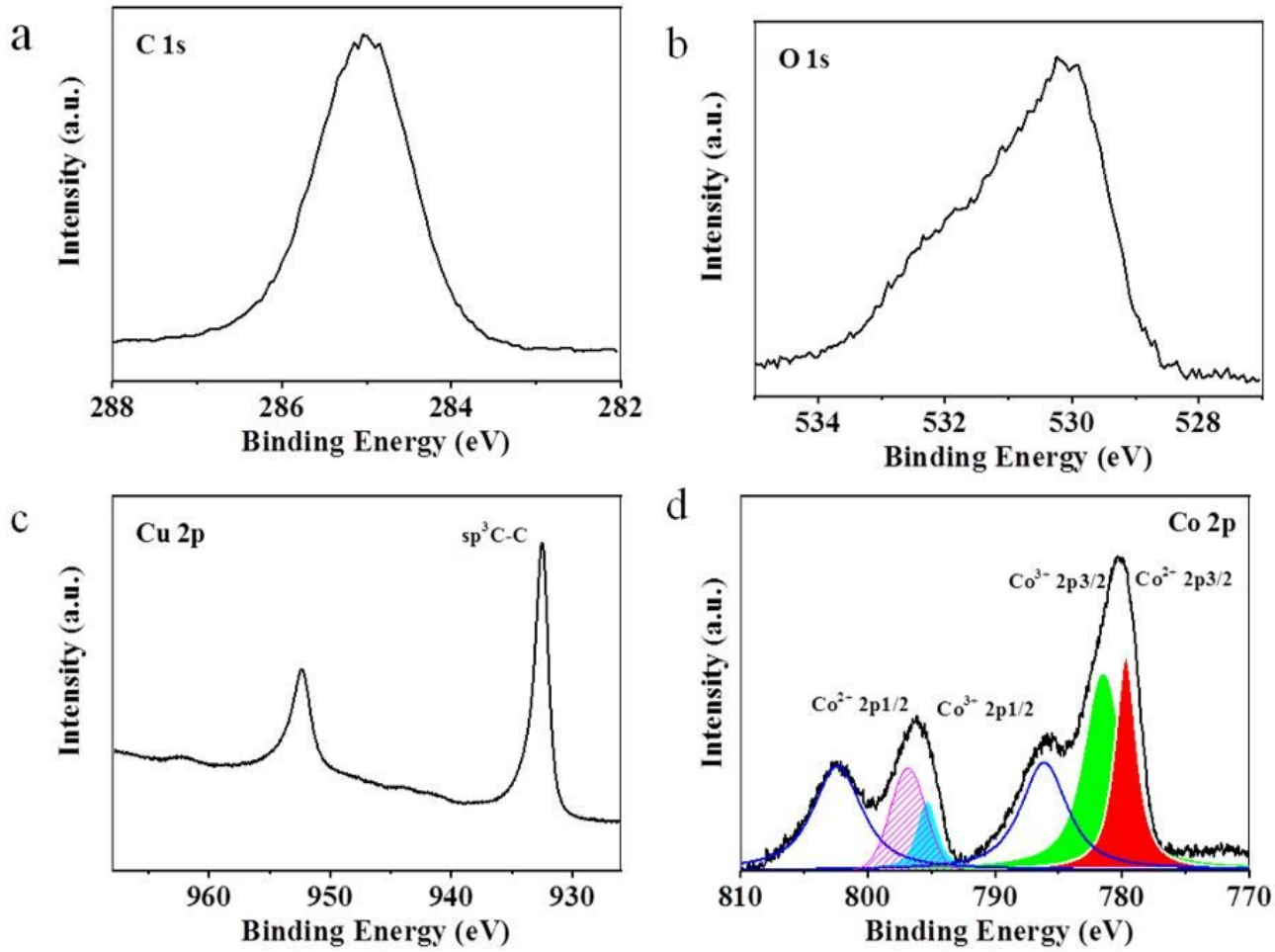

Figure 4

XPS analysis of $CuCo_2O_4$ MMOFs. (a) C 1s; (b) O 1s; (c) Cu 2p; (d) Co 2p.

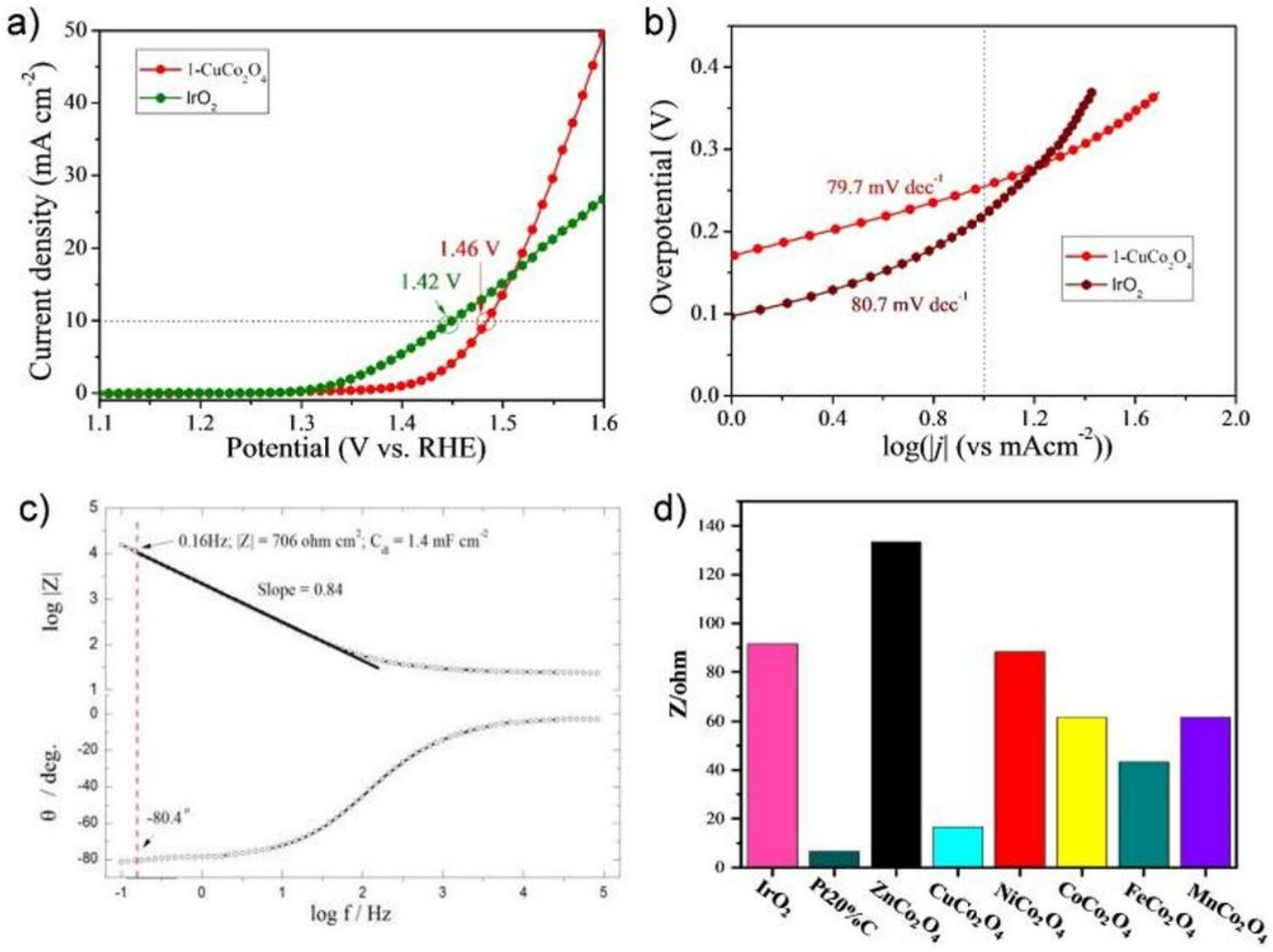

Figure 5

a) Electrochemical surface area (ECSA) corrected OER LSV curves and its corresponding b) Tafel plots of different electrodes ($CuCo_2O_4$, IrO_2) without iR compensation at a sweep rate of 5 mV•s^{-1}. c) Typical Bode plot $CuCo_2O_4$ electrodes vs. HgO/Hg, in 1M KOH at 25 ℃ (geometrical area: 0.07065 cm^2). d) Results of impedance measurements on Spinel in 1M KOH at 25℃

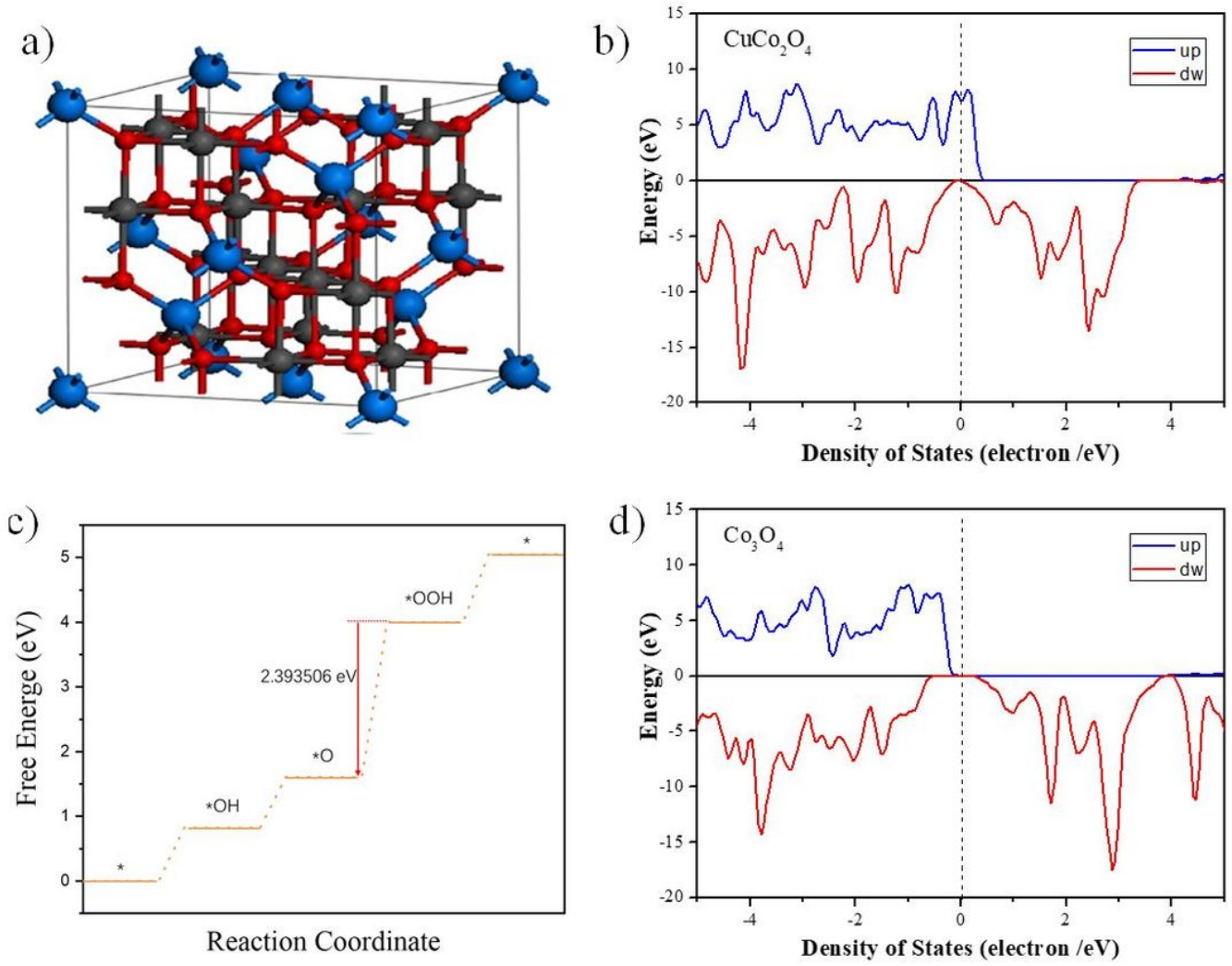

Figure 6

a) Crystal structure of $CuCo_2O_4$. b) The calculated density of states (DOS) of $CuCo_2O_4$. c) Density functional theory calculation for the OER mechanism. a Free energy diagram for OER on $CuCo_2O_4$. d) The calculated density of states (DOS) of Co_2O_3.